Global Journal of Environmental Science and Management
(GJESM)

Homepage: https://www.gjesm.net/

Podcasts

ORIGINAL RESEARCH ARTICLE

Environmental floods assessment by integrating satellite-based water classifications with local hydroclimatic and groundwater observations

A.B. Umirbayeva[1,*], E.O. Orynbassarova[2], Y.S. Auyelkhan[3], N. Saburova[4], Y. Pangaliyev[5]

[1]*Department of Geodesy and Cartography, Cadastre, International Educational Corporation, 050043, Almaty, Kazakhstan*

[2]*Geomatics Innovation Center, Satbayev University, 050013, Almaty, Kazakhstan*

[3]*Geology and Oil-Gas Business Institute named after K. Turyssov, Satbayev University, 050013, Almaty, Kazakhstan*

[4]*Department of Hydrogeology, Engineering and Petroleum Geology, Satbayev University, 050013, Almaty, Kazakhstan*

[5]*Department of Ecology and Life Safety, Faculty of Engineering, Yessenov University, 130000 Aktau, Kazakhstan*

ARTICLE INFO

Article History:
Received 21 July 2026
Revised 24 September 2026
Accepted 29 October 2026

Keywords:
Environmental flood assessment
Freeze–thaw
Groundwater heterogeneity
Hydroclimatic variability
Optical remote sensing
Surface water

ABSTRACT

BACKGROUND AND OBJECTIVES: Flood response in the lower Zhem River basin depends on conditions across different spatial and temporal scales. The study objectives were to investigate whether regional satellite-derived surface water mapping, meteorological records from proximity monitoring stations near Kulsary and local groundwater observations provide a consistent basis for the environmental assessment of the April 2024 flood event. The analysis separated observed water-area dynamics from unmeasured hydraulic mechanisms.

METHODS: Daily meteorological observations from three stations covering 2016 to 2025 were analyzed together with regional optical satellite images acquired during 2021 to 2025, eleven higher-resolution optical images from March to April 2024, three matched radar–optical comparisons and 2024 monitoring records from sixteen urban groundwater wells. Optical water surface areas were quantified using a fixed green-to-near-infrared water-index threshold. Seasonal rankings, acquisition-date offsets relative to a published upstream stage maximum, classified area changes and conditional water-table equivalent indices were evaluated descriptively, with explicit accounting for variations in sensor footprints and observation timing.

FINDINGS: The largest classified regional surface-water area was 622.35 square kilometers on 11 April 2024, including pre-existing water. Local seasonal snow depths of 8 to 12 centimeters and precipitation totals of 27.3 to 36.2 millimeters were not recorded within the available station records. The published upstream stage maximum preceded the regional and higher-resolution observed water-area maxima by nine and twelve days, respectively. An evaluation of three optical–radar pairs revealed an overall agreement of 92.1 percent alongside a water-class harmonic mean score of 69.5 percent, highlighting notable divergence in classification discrepancies. Recorded groundwater depths ranged from 0.37 to 5.53 meters. The higher-resolution series showed a 63.96 percent area contraction between 14 and 18 April.

CONCLUSION: The evidence identifies substantial satellite-observed water-area change alongside lower-basin meteorological contrasts and heterogeneous urban groundwater conditions. Hile these observations support environmental flood monitoring, the explicit partitioning of surface runoff, drainage pathways, and groundwater exchange remains unresolved. Operational assessment requires independently validated water maps, matched observation footprints and time-resolved river and groundwater records.

DOI: https://doi.org/10.22034.gjesm.2027.02.11

This is an open access article under the CC BY license (http://creativecommons.org/licenses/by/4.0/)

NUMBER OF REFERENCES	NUMBER OF FIGURES	NUMBER OF TABLES
34	6	10

*Corresponding Author:
Email: a.umirbaeva@kazgasa.kz
Phone: +7 708 717 30 89
ORCID: 0000-0002-4746-3411

Note: Discussion period for this manuscript open until June 01, 2027 on GJESM website at the “Show Article”.

INTRODUCTION

Spring floods in semi-arid continental basins reflect the temporal and spatial distribution of snowmelt and rainfall, river routing, land-surface conditions and floodplain connectivity (Alfian et al., 2026). The April 2024 flood at Kulsary, Zhylyoi District of Atyrau Oblast, caused substantial damage. Contemporary accounts documented extensive residential damage and demographic displacement throughout the emergency flood response in Kazakhstan (ACAPS, 2024). The consequences of flooding also highlight the importance of understanding community-level vulnerability and adaptive capacity when evaluating flood impacts and responses (Depari, 2026). Establishing the mechanisms responsible for the affected area requires distinguishing meteorological input in the lower basin from discharge delivered by the upstream Zhem River catchment and separating remotely sensed open water from new flood inundation. The area mapped as water is a classified surface, not a direct measure of newly inundated land or floodwater volume. In low-relief terrain a given volume may cover very different areas depending on topography, connectivity, pre-existing water, river stage and surface conditions. Similarly, variations in groundwater depth and ground-surface thermal conditions may correlate with inundation extent without explicitly distinguishing between infiltration and drainage fluxes. The present analysis therefore evaluates observational contrasts and the extent to which they constrain environmental flood assessment by aligning upstream-stage dates, classified-water changes and local groundwater conditions. The integration gap concerns differences in spatial support, timing and physical units rather than the availability of multiple datasets alone. The hydrological response of frozen soils to snowmelt exhibits substantial variability; although soil freezing can attenuate infiltration capacity, it does not inherently render the surface impermeable. Gray *et al.* (2001) classified frozen soil profiles according to their infiltration characteristics. In unlimited profiles, gravity flow dominates and most meltwater enters the soil. Limited profiles are controlled mainly by capillary flow, and infiltration varies with antecedent soil moisture, ice content, and initial soil temperature. In restricted profiles, ice lenses, saturated ice-filled pores, or similar near-surface conditions can greatly reduce water entry. Field observations from the Canadian Prairies show that meltwater may infiltrate through air-filled macropores even when the surrounding soil remains frozen (Mohammed *et al.*, 2018). The infiltration response is fundamentally governed by antecedent soil profile conditions during snowmelt; consequently, restricted near-surface permeability retains a greater proportion of meltwater at the surface, driving enhanced runoff generation (Zhao and Gray, 1999; Granger *et al.*, 1984). Flood development may also be affected by groundwater storage and drainage. A shallow water table leaves less available storage in the unsaturated zone and increases the possibility of groundwater reaching the land surface (Hughes *et al.*, 2011; Abboud *et al.*, 2018). Such groundwater contributions can affect both the extent and duration of inundation. During overbank flooding, surface water can also recharge floodplain aquifers, creating exchange between surface water and shallow groundwater (Doble *et al.*, 2014; Nowinski *et al.*, 2012). The significance of these hydrological mechanisms is well-documented in other low-relief regions; for instance, agricultural water-table elevation in the South American plains corresponded with a twofold expansion in inundation extent (Houspanossian *et al.*, 2023). Groundwater-related urban flooding associated with restricted drainage has also been documented in northern Almaty, Kazakhstan (Mirlas *et al.*, 2025). Saline and sodic soils occur across the Caspian Lowland and may exhibit reduced hydraulic conductivity under structural and wetting conditions (Adeyemo *et al.*, 2022). Neither conductivity nor event-time

infiltration was directly determined at Kulsary; these properties are considered candidate controls rather than established causes of the observed flooding. The analysis addresses three research questions that separate observable environmental conditions from mechanistic attribution:

Research question 1 **(**Q1**):** local meteorological context. Were 2024 snow-depth and March–April precipitation observations recorded at the three lower-basin anomalously elevated relative to their available 2016–2025 baseline records? While this rank-based comparison evaluates the distinctiveness of local station conditions; complete source apportionment further necessitates catchment-scale discharge and water-balance monitoring.

Research question 2 **(**Q2**):** antecedent surface thermal conditions. Was the observed 2024 near-surface freeze–thaw sequence distinctive relative to the selected comparison years? Soil-surface temperature describes near-surface thermal variability; its hydraulic interpretation requires depth-resolved soil observations.

Research question 3 **(**Q3**):** groundwater heterogeneity and surface-water contraction. How variable were groundwater depths and conditional water-table equivalent indices among monitored urban sites, and how did classify surface-water area change relative to the published upstream stage chronology? These are site-level and area-based characterizations rather than definitive evaluations of floodplain-wide storage capacity or drainage efficiency.

Satellite observations were used to describe the spatial development of classified surface water. Optical water indices are widely applied for open-water mapping, including the green–near-infrared formulation introduced by McFeeters (1996). Prior studies have documented their applicability within arid and semi-arid floodplains environments (Mohammadi *et al.*, 2017). Sentinel-2 provided a multi-year record for comparing the 2024 event with previous years. PlanetScope imagery captured changes during flood expansion and recession at shorter time intervals, while Sentinel-1 (S1) synthetic aperture radar (SAR) provided a separately generated water classification and observations under cloudy conditions (Munasinghe *et al.*, 2018). Similarly, methodological assessments of remote-sensing indicators emphasize context-specific validation, cross-sensor harmonization, and the cautious interpretation of image-derived proxies (Mkilima *et al.*, 2027; Zhidebayeva *et al.*, 2025). Satellite data have been used for operational flood monitoring in Kazakhstan (Arkhipkin and Sagatdinova, 2016), primarily for mapping affected areas and assessing damage. Investigations that integrate satellite observations with groundwater monitoring records to evaluate flood dynamics remain relatively limited (Zagidullina and Kulebayev, 2024). Laiskhanov *et al.* (2025) examined the same 2024 event at the basin scale and mapped 836.8 square kilometers (km^2) of inundation. Their findings attributed the flooding event to anomalous winter snow accumulation combined with rapid thermal warming within the upstream catchment. The present study focuses on Kulsary and the lower part of the basin, where local meteorological and groundwater observations add receiving-landscape context to the regional water-area chronology. The study aimed to compare lower-basin station conditions relative to their multi-year distributions, align within-event water classifications with published upstream-stage timing, assess radar–optical correspondence, and characterize sampled groundwater variability in support of environmental flood monitoring. This study is performed for Kulsary and the lower Zhem (Emba) basin, western Kazakhstan, using observations spanning 2016–2025 and focusing on the April 2024 flood.

MATERIALS AND METHODS

Study area

Kulsary lies in the northeastern Caspian Lowland within the lower Zhem (Emba) River basin. The study area features subdued topographic relief, a pronounced continental climate, fine-textured sediment and spatially heterogeneous shallow

groundwater. These biophysical attributes render the receiving landscape particularly well-suited for evaluating floodwater persistence and waterlogging dynamics. The low-relief terrain includes shallow depressions and poorly graded pathways that can favor water accumulation under some flow conditions (Ongayev *et al.*, 2026). Winters are cold and snow cover is generally shallow, with seasonal warming during March and April. Snow depth, ground-temperature history and soil moisture can modify runoff timing and infiltration (Zhang, 2005). Near-surface materials include loams, sandy loams and locally clay-rich horizons; salinity and sodicity may influence soil hydraulic properties (Adeyemo *et al.*, 2022). Fig. 1 locates the study area; satellite-scene coverage areas are reported separately. This framework enables the comparative analysis of a regional satellite signal against lower-basin atmospheric conditions and urban groundwater measurements, whereas hydraulic attribution is evaluated independently.

Datasets

The analysis uses the datasets listed in Table 1. Daily meteorological observations for 2016–2025 came from the available Kazhydromet stations at Kulsary, Karabau and Inderborskiy, including air temperature, soil-surface temperature at zero centimeters (0 cm), precipitation, snow depth and relative humidity; these stations describe Kulsary and regional lower-basin conditions rather than the upstream runoff-generation area. Sentinel-2 MultiSpectral Instrument (MSI) Level-2A (L2A) imagery was used to classify open-water area during 2021–2025 within a nominal 12,052 km² regional footprint at 10 m resolution. These products were provided through the European Space Agency (ESA) Copernicus program. Eleven approximately 3 m PlanetScope scenes supplied by Planet Labs, a public benefit corporation (PBC), and acquired from 30 March to 20 April 2024 covered a separate 341 km² subset. Available imagery was retained to characterize surface expansion and contraction across irregular acquisition intervals, with both sensor footprints analyzed independently. The reported imagery-derived quantities are classified water areas, not inherently newly inundated land. Sentinel-1 ground range detected (GRD) imagery in interferometric wide (IW) mode with vertical–vertical (VV) polarization was classified independently of the optical masks for a cross-sensor correspondence assessment. No radar acquisition within three days of the 11 April Sentinel-2 maximum was included in the matched pairs. Groundwater data comprised 2024 measurements of water-table depth, mineralization, and hydraulic head across sixteen urban wells, alongside separate 2023–2024 observations acquired from regional floodplain monitoring stations. The wells belong to the available urban monitoring network rather than a spatially stratified floodplain survey. Because individual urban-well sampling dates could not be synchronized with flood progression (arrival, peak, and recession) and given the absence of event-scale piezometric records across both monitoring networks, the separate floodplain observations serve primarily to establish interannual context rather than an immediate pre-event baseline.

Optical water classification

Open water was classified using the normalized difference water index (NDWI), calculated from green and near-infrared (NIR) reflectance using Eq. 1 (McFeeters, 1996). Because the computational approach alone cannot differentiate permanent surface water from newly inundated areas, this differentiation necessitates a verified pre-event water mask applied across an identical valid footprint.

$$\mathrm{NDWI} = \frac{\mathrm{Green} - \mathrm{NIR}}{\mathrm{Green} + \mathrm{NIR}} \quad (1)$$

NDWI was thresholded at values greater than zero (NDWI > 0) for each optical acquisition. The threshold is a nominal open-water rule rather than a sensor- or season-calibrated optimum. Shallow or turbid water, saline flats, built surfaces, cloud shadows and mixed pixels may be incorrectly classified, particularly under heterogeneous surface and atmospheric conditions.



Fig. 1: Geographical location of Kulsary in western Kazakhstan and the lower Emba–Caspian Lowland, with geographical context and reported study-area coverage (Sentinel-2: 12,052 km²; PlanetScope: 341 km²), and acquisition-boundary polygons are not shown

Table 1: Observational datasets, spatial and temporal coverage, and their evidentiary roles. Groundwater measurements from urban wells and floodplain sites are distinct networks

Dataset	Source	Coverage	Spatial resolution / monitoring network	Role in analysis
Air temperature	Kazhydromet	2016–2025, daily	3 stations	Spring warming context (Q2)
Soil surface temperature (0 cm)	Kazhydromet	2016–2025, daily	3 stations	Selected-year surface freeze–thaw context (Q2)
Precipitation	Kazhydromet	2016–2025, daily	3 stations	Local precipitation context; 2024 rank (Q1)
Snow depth	Kazhydromet	2016–2025, daily	3 stations	Local snow-depth context; 2024 rank (Q1)
Relative humidity	Kazhydromet	2016–2025, daily	3 stations	Climatic characterisation
Sentinel-2 MSI (L2A)	ESA Copernicus	2021–2025	10 m; 12,052 km² footprint	Five-year classified open-water maxima; interannual comparability unverified
PlanetScope	Planet Labs PBC Planet Labs PBC, (2026)	30 Mar – 20 Apr 2024	~3 m; 341 km² footprint	Within-footprint classified water chronology; acquisition-quality sensitivity
Sentinel-1 GRD (IW, VV)	ESA Copernicus	Jul–Sep 2023 reference; Apr 2024	10 m	Cross-sensor correspondence, not independent validation
Groundwater, urban wells	Regional hydrogeological monitoring	2024	16 observation wells within the Kulsary urban area	Sampled groundwater state; conditional equivalent index I
Groundwater, floodplain sites	Regional hydrogeological monitoring	2023–2024	Floodplain monitoring sites outside the town	Interannual site-level context; not an event hydrograph

By substituting near-infrared reflectance with shortwave-infrared bands, the modified normalized difference water index enhances surface water delineation in complex urban and built-up environments (Xu, 2006). Because PlanetScope products lack a corresponding shortwave-infrared band, the green–near-infrared index was retained. Sentinel-2 and PlanetScope nonetheless differ in spectral response and pixel size. Although a visual inspection of the true-color scenes revealed notable spatial inconsistencies, this qualitative evaluation did not constitute a formal accuracy assessment. Corresponding band assignments are detailed in Table 2. Sentinel-2 band 3 (B3) and band 8 (B8) represent the green and NIR channels; PlanetScope uses band 2 (B2) and band 4 (B4) in four-band products, or B4 and B8 in eight-band products (Planet Labs PBC, 2026). Optical processing was performed using ArcGIS Pro 3.2, a geographic information system (GIS) platform. The documented workflow calculated NDWI from green and near-infrared bands, generated a binary open-water mask at NDWI > 0, polygonised the classified pixels and calculated area in square kilometres (Fig. 2). Although a pre-event persistent-water baseline was not subtracted, long-term water-occurrence and seasonality datasets can provide valuable constraints for baseline selection (Pekel *et al.,* 2016). Scene-specific identifiers, quality-mask classes, valid-area denominators, georegistration parameters, and the delivered PlanetScope asset type were absent from the analytical record; consequently, common-footprint masking and band configuration require explicit verification. Furthermore, threshold sensitivity and independent reference accuracy remain uncalculated, necessitating probability sampling of reference labels to quantify classification error and spatial and area uncertainty (Olofsson *et al.,* 2014). Representative index images appear in the corresponding Fig. 3.

Radar classification and cross-sensor comparison

The radar classification used the median of corresponding-orbit July–September 2023 scenes as a dry-season reference. Pixels were classified as water when vertical–vertical backscatter decreased by more than 4 decibels (dB) relative to the reference and was below −14 dB; a 30 meters (m) focal median filter was applied; the recorded thresholds were not calibrated against independent water labels. Three optical–radar pairs were compared on 2 April, 14 April and 18–19 April 2024 over their overlapping usable pixels on a nominal 10 m grid. A temporal separation of up to one day may encompass actual dynamics in water-boundary configuration. For each image pair, water and non-water concordance was evaluated using overall agreement, Cohen's kappa (κ), water-class intersection over union (IoU) and the F1 score (representing the harmonic mean of precision and recall), with the NDWI mask serving as the reference for directional precision and recall. The radar and optical masks are both classifications; these are cross-sensor correspondence statistics rather than independently validated mapping accuracy. Precise orbit and product identifiers, radiometric and terrain corrections, as well as resampling and spatial alignment configurations, remain essential for achieving numerical reproduction.

Snow depth and precipitation characterization

Maximum snow depth and total March–April precipitation were evaluated separately at each station. The snow-depth maxima are not necessarily contemporaneous with flood arrival, and the two-month precipitation period includes dates after flood onset. Converting snow depth to equivalent precipitation risks double-counting snowfall when aggregating data across disparate observation periods. Consequently, the combined snow-plus-precipitation metric was omitted from the analysis, and neither station variable was converted into an event runoff volume.

Table 2: Product-dependent green and near-infrared band assignments for the NDWI calculation

Index	Formula	Sentinel-2 bands	PlanetScope product bands
NDWI	(Green − NIR)/(Green + NIR)	B3, B8	Four-band: B2, B4; eight-band: B4, B8

Note: Bands are listed in the order in which they appear in the formula; the PlanetScope asset type must be established from the delivered metadata before either band pair is assigned to the eleven-date sequence

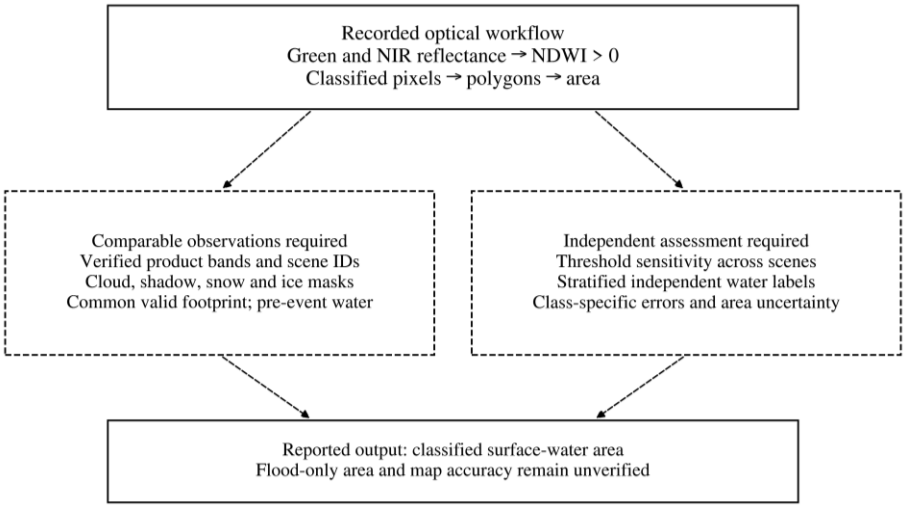

Fig. 2: Optical processing sequence used to obtain classified open-water area; dashed elements identify additional quality-control and validation requirements

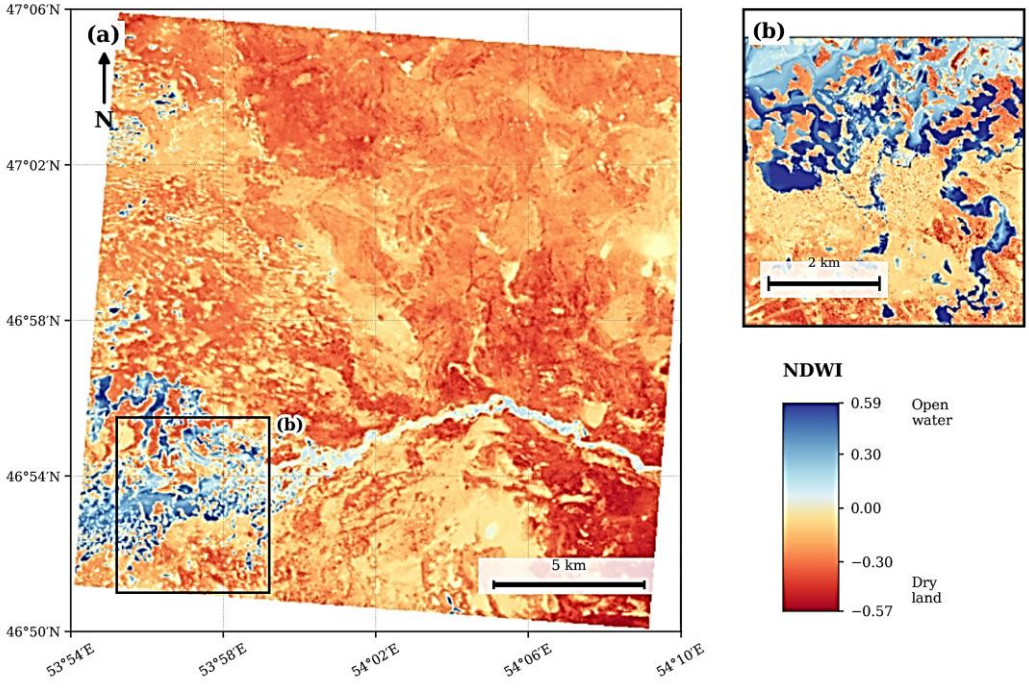

Fig. 3: Examples of the green–near-infrared water-index imagery for the Kulsary region. Areas displayed as water are classifications, not independently verified flood-only extents

Conditional water-table equivalent index

For each urban well, a conditional equivalent index computed as depth to water multiplied by assumed specific yield (SY) and a meter-to-millimeter conversion. Depth to groundwater is denoted by d, measured in meters, and SY, a dimensionless parameter. Values of 0.05 and 0.10 were retained as sensitivity scenarios rather than site-calibrated aquifer properties, using Eq. 2 (Johnson, 1967). The index is not measured unsaturated-zone storage, infiltration capacity or flood-related groundwater-storage change.

$$I = 1{,}000 \times d \times S_Y \quad (2)$$

Freezing, antecedent moisture, pore connectivity, stratification and event-time water-table movement can alter actual water entry. SY characterizes drainage near the water table and need not equal the accessible pore deficit in an unsaturated profile. These calculations reflect local parameter-scale variability among the sixteen monitoring sites only, exhibiting a direct proportional scaling relationship where doubling SY doubles I. Furthermore, the results lack comparison with aggregated snow-precipitation inputs and are not scaled to the regional domain (Johnson, 1967; Ma *et al.*, 2024).

Statistical analysis and uncertainty

Observations comprise meteorological station records, satellite classifications and groundwater monitoring values. Calculated summaries include arithmetic means, medians, sample standard deviations (SD), station ranks, classified areas, calendar offsets, optical–radar correspondence and conditional indices; station ranks equal one plus the number of annual values exceeding 2024, with ties sharing a rank. These summaries do not quantify floodwater volume, surface runoff, infiltration rates, or groundwater-exchange fluxes. Inferential statements are therefore restricted to descriptive results for the stated Table 3 periods, without significance levels or pixel-based confidence intervals; optical area processing used ArcGIS Pro 3.2 and table arithmetic was independently checked using Python 3.12 and NumPy. Q1 was evaluated from the 2024 station snow-depth and March–April precipitation ranks within the available 2016–2025 records. Q2 compares 0 cm soil-surface temperatures during 1 March–5 April for 2016, 2019, 2022 and 2024 using days with mean temperature at or below zero degrees Celsius (≤0 °C), sub-zero minima and within-day freeze–thaw transitions; this comparison is descriptive because the selected subset does not span all eligible years. Q3 evaluates measured groundwater depths alongside conditional equivalent indices across the sixteen urban locations, while independently aligning temporal shifts in the PlanetScope classified-water area with the published 2 April upstream stage maximum (Laiskhanov *et al.*, 2025). Annual descriptive summaries and rankings for station snow depth and precipitation are presented in Table 3. Consecutive classified-area differences were divided by elapsed acquisition interval, with proportional surface contraction expressed as 100 × (Aearlier − Alater)/Aearlier. The four-year thermal subset is not treated as a climatology of all years in 2016–2025. Sentinel-2 annual maxima are descriptive maxima from available acquisitions; calendar offsets subtract 2 April 2024 from satellite dates and are not measured hydraulic travel times. Because spatially autocorrelated comparison pixels do not satisfy the assumption of independent replication, agreement statistics are reported descriptively without pixel-based confidence intervals, whereas the rounded April 14 contingency matrix was verified arithmetically.

RESULTS AND DISCUSSION

Local station conditions and upstream snowmelt context

Maximum recorded winter snow depth for 2023–2024 was 8 cm at Kulsary, 10 cm at Karabau and 12 cm at Inderborskiy. March–April precipitation totals were 27.3, 27.5 and 36.2 mm, respectively (Table 3). The rank positions in the

Table 3: Maximum snow depth and cumulative March–April precipitation at three stations, 2016–2025, with 2024 ranks

Year	Kulsary snow (cm)	Kulsary precipitation (mm)	Karabau snow (cm)	Karabau precipitation (mm)	Inderborskiy snow (cm)	Inderborskiy precipitation (mm)
2016	19	102.8	26	—	15	—
2017	15	20.3	23	24.1	36	30.0
2018	12	17.8	10	38.0	13	41.1
2019	6	64.0	24	29.8	24	50.7
2020	7	38.1	5	32.3	4	12.4
2021	8	6.1	18	50.4	18	47.4
2022	9	60.2	18	56.7	8	37.6
2023	12	13.4	20	24.3	44	26.7
2024	8	27.3	10	27.5	12	36.2
2025	17	65.2	19	37.9	12	22.0
Mean	11.3	41.5	17.3	35.7	18.6	33.8
SD	4.5	30.6	6.8	11.4	12.6	12.3
Median	10.5	32.7	18.5	32.3	14.0	36.2
Min–max	6–19	6.1–102.8	5–26	24.1–56.7	4–44	12.4–50.7
Rank of 2024 (1 = highest)	7 of 10	6 of 10	8 of 10	7 of 9	7 of 10	5 of 9

Note: Snow-depth observations cover 2016–2025 (n = 10) at each station. March–April precipitation covers 2016–2025 at Kulsary (n = 10) and 2017–2025 at Karabau and Inderborskiy (n = 9). A dash denotes a year outside the stated precipitation series. Rank 1 is the highest value; ties share a rank.

available records show that 2024 was not distinguished by unusually high local station snow depth or two-month precipitation. While these observations characterize the local meteorological context; they do not quantify runoff volumes generated within the lower catchment. At Kulsary, March–April 2024 precipitation ranked sixth highest among ten observations and maximum winter snow depth ranked seventh, while station data exhibit considerable interannual variability (Table 3). At Karabau and Inderborskiy, 2024 snow-depth ranks were eighth and seventh, and precipitation ranks were seventh and fifth, respectively. These values reflect prevailing lower-basin environmental conditions rather than quantifying specific floodwater-source fractions. Published basin-scale analysis reported winter 2023–2024 precipitation approximately 44–49% (percent) above the long-term average in the Aktobe headwaters, upper-basin snow depths reaching approximately 0.8 m and a water-level maximum of 415 cm at Zhagabulak on 2 April (Laiskhanov *et al.*, 2025). While the observed upstream–local contrast provides a compelling rationale for catchment-wide monitoring, it does not explicitly apportion incoming river discharge from locally generated surface runoff.

Interannual comparison of antecedent soil-surface thermal conditions

The available common-window comparison at Kulsary used observations for 2016, 2019, 2022 and 2024 during 1 March–5 April (Table 4). Thermal notation defines mean soil-surface temperature (Tsoil), daily mean soil-surface temperature (Tmean), daily minimum soil-surface temperature (Tmin) and daily maximum soil-surface temperature (Tmax); the less-than symbol (<) indicating values falling below the specified threshold. Mean soil-surface temperature was ≤0 °C on 11 days in 2024, compared with 2, 2 and 12 days in 2016, 2019 and 2022; corresponding within-day freeze–thaw counts were 20, 7, 18 and 21 days. In 2024, daily mean soil-surface temperature last reached ≤0 °C on 14 March, while sub-zero minima persisted intermittently until 30 March. The corresponding final dates of sub-zero daily minima occurred on 23 March 2016, 1 April 2019, 29 March 2022, and 30 March 2024. These records indicate recurrent March surface freeze–thaw cycles rather than persistent surface freezing into April, with potential implications for snowmelt infiltration, near-surface soil moisture redistribution and subsequent runoff generation under variable antecedent conditions.

Table 4: Antecedent soil-surface thermal conditions at Kulsary, 1 March–5 April

Year	Mean Tsoil (°C)	Days Tmean ≤0 °C	Days Tmin <0 °C	Freeze–thaw days	Last Tmean ≤0 °C	Last Tmin <0 °C
2016	6.14	2	7	7	17 Mar	23 Mar
2019	6.33	2	18	18	4 Mar	1 Apr
2022	3.75	12	21	21	21 Mar	29 Mar
2024	4.64	11	20	20	14 Mar	30 Mar

Note: A freeze–thaw day was defined as a day with Tmin < 0 °C and Tmax > 0 °C. Summary statistics were calculated over the common 36-day period of 1 March–5 April; a complete decade-wide comparison would require all ten daily series under the same eligibility rule, such as at least 33 valid days in each window

The 2024 observations do not indicate a uniquely late soil-surface thaw among these selected years. Similar thermal indices occurred in 2022, when regional classified-water area was smaller. The comparison establishes thermal non-uniqueness across the four-year subset; furthermore, soil permeability and event-scale infiltration remain distinct physical quantities that necessitate concurrent observations of profile temperature, moisture, ice and infiltration dynamics (Gray *et al.*, 2001; Mohammed *et al.*, 2018).

Interannual Sentinel-2 classified surface-water area

Within the nominal 12,052 km² Sentinel-2 study footprint, the largest classified water area in the examined 2021–2025 scenes were 622.35 km² on 11 April 2024 (Table 5). The mean of the other four observed-scene maxima was 110.87 km², giving a descriptive ratio of 5.61. This analysis provides a comparative evaluation of available classifications rather than a statistically tested interannual flood-magnitude ratio. Because pre-existing water surfaces were not subtracted, variations in acquisition timing and usable coverage constrain the accurate capture of flood peaks.

PlanetScope chronology of classified surface-water area

Eleven PlanetScope scenes provide a higher-temporal-resolution description of classified water within the separate 341 km² footprint (Table 6 and Fig. 4). The mapped area of interest (AOI) is identified in the satellite panels. Uneven observation intervals are reported in days (d), with arithmetic area-change rates in square kilometers per day (km²/d); Table 6 also aligns each acquisition with the published 2 April upstream stage maximum. Although these temporal offsets link the observation systems without estimating flood-wave velocity, the intervening areas inherit scene-quality and band-provenance uncertainties that preclude rescaling to the regional Sentinel-2 footprint. Classified surface-water area increased from 8.49 km² on 30 March to 73.58 km² on 14 April, an 8.67-fold difference within the monitored subset. The 10–11 April pair showed an increase of 18.49 km² over one day. The 4 April area (12.38 km²) was lower than on 3 April (17.19 km²); intervals using this scene are flagged because their comparability has not been established. Using the published 2 April upstream stage maximum as a temporal baseline, the 7 April expansion, 11 April regional peak, and 14 April subset maximum occurred at calendar offsets of 5, 9 and 12 days, respectively (Laiskhanov *et al.*, 2025). These temporal values represent acquisition-date offsets rather than true hydraulic travel times between observations. Within the subset, classified area declined from 73.58 km² on 14 April to 26.52 km² on 18 April, a 63.96% reduction (47.06 km²) over four days and an arithmetic rate of −11.77 km²/d. The 20 April area was 27.04 km², indicating a near-stable classification over the final two-day interval rather than continued monotonic contraction.

Table 5: Annual observed-scene maximum classified surface-water area from available Sentinel-2 observations, 2021–2025, within the nominal 12,052 km² footprint

Year	Observed-scene maximum classified water (km²)
2021	19.65
2022	161.32
2023	113.46
2024	622.35
2025	149.04

Note: Values include any classified persistent water; usable coverage and peak-detection opportunity differ among years

Table 6: PlanetScope classified-water area within the nominal 341 km² footprint, with acquisition intervals, arithmetic area-change rates and calendar offsets from the published upstream stage maximum on 2 April 2024*

Date	Interval since previous acquisition (d)	Classified water area (km²)	Mean rate since previous acquisition (km²/d)	Offset from 2 April (d)
30 Mar 2024	—	8.49	—	-3
2 Apr 2024	3	10.00	+0.50	0
3 Apr 2024	1	17.19	+7.19	1
4 Apr 2024 *	1	12.38	uncertain*	2
7 Apr 2024	3	53.19	uncertain*	5
10 Apr 2024	3	48.86	−1.44	8
11 Apr 2024	1	67.35	+18.49	9
12 Apr 2024	1	71.00	+3.65	10
14 Apr 2024	2	73.58	+1.29	12
18 Apr 2024	4	26.52	−11.77	16
20 Apr 2024	2	27.04	+0.26	18

*The 4 April classification has unverified scene comparability. Rates spanning 3–4 and 4–7 April are excluded from hydrological interpretation. Offsets are calendar differences from the published upstream stage maximum, not hydraulic travel times.

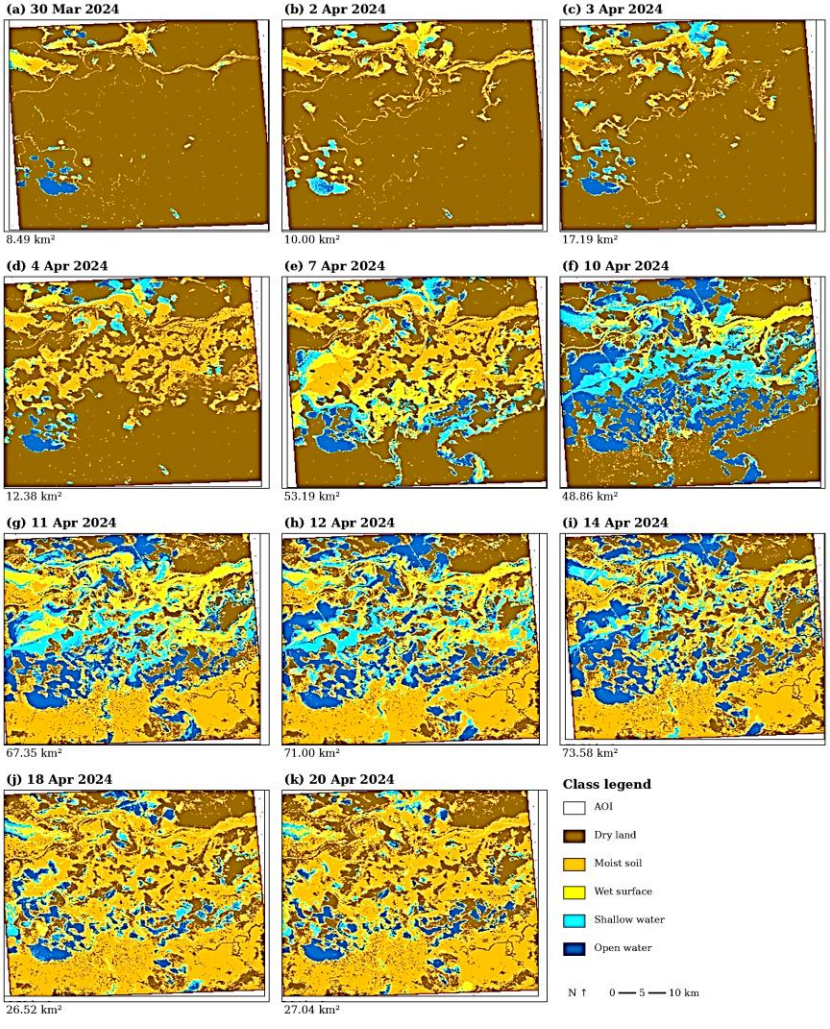

Fig. 4: PlanetScope-based water classifications on eleven dates from 30 March to 20 April 2024. Panels depict scene-specific classified water; product-band provenance and common valid coverage require verification

Optical–radar classification correspondence

For the three matched optical–radar image pairs, acquisition time separation is denoted by Δt and the comparison sample size is reported in pixels (px), with 10^6 px representing one million pixels. Overall pixel agreement was 92.1%, Cohen's κ was 0.65, water-class intersection over union was 53.3% and the F1 score was 69.5% (Table 7). Overall agreement is disproportionately influenced by the predominant non-water class, whereas the water-specific metrics reveal substantial disagreement. Furthermore, these figures represent cross-sensor correspondence statistics rather than formal measures of classification accuracy, as neither product underwent independent validation. Crucially, no matched pair captured the 11 April Sentinel-2 maximum. On 14 April, the radar mask labelled 16.2% of the compared footprint as water, compared with 25.3% in the optical mask. When the optical mask is used only as a comparison reference, radar water-class precision was 92.3% and recall 59.1%, giving F1 = 72.0% (Table 8). The corresponding omission fraction relative to the optical reference label was 40.9%, illustrating asymmetric inter-sensor disagreement rather than establishing the absolute accuracy of either platform. Shallow inundation, roughness, vegetation, mixed pixels, saline surfaces and cloud masking may affect the masks (Munasinghe *et al.*, 2018). Fig. 5 displays the products separately, whereas Tables 7 and 8 refer to their reported common comparison footprint.

Urban groundwater heterogeneity and conditional equivalent indices

Groundwater depth at the sixteen monitored urban wells ranged from 0.37 to 5.53 m (mean 2.62 m; median 2.43 m; standard deviation 1.38 m). Three measured groundwater depths fell below 1 m and four below 1.5 m; these values represent proportions of the sampled monitoring wells rather than fractions of total urban land area. Mineralization ranged from 1.8 to 21.6 grams per liter (g/L) (median approximately 6.95 g/L), and twelve wells exceeded 3 g/L (Table 9). In the absence of exact dates linked to flood progression, these measurements cannot resolve pre-event baseline water levels or quantify subsurface groundwater response during inundation. Under specific-yield scenarios of 0.05 and 0.10, I ranged from 18.5 to 276.5 mm and from 37.0 to 553.0 mm, respectively (Table 9). The twofold change follows directly from the assumed parameter and does not represent an empirically estimated uncertainty interval. The separate floodplain monitoring locations recorded groundwater depths of 1.43–3.08 m in 2023 and 0.29–1.51 m in 2024, with reported annual fluctuation of 0.35–2.10 m. While these records characterize interannual variability across monitored sites, they do not resolve subsurface groundwater dynamics during the April 14–18 surface area contraction. Urban wells 306, 307 and 317 had depths below 1 m and identify locations for targeted hydraulic investigation. Because the limited sample size yields no area-weighted estimate of shallow, it remains inconclusive groundwater storage increased or decreased during the period of surface water contraction.

Synthesis of the research questions

Table 10 distinguishes the observational results from untested mechanisms. Local meteorological ranks (Q1), selected-year surface thermal variability (Q2) and urban groundwater heterogeneity plus classified-water chronology (Q3) are integrated by observation scale and timing. The resulting environmental assessment identifies the quantities relevant to monitoring while separating water-area observations from runoff, infiltration and drainage fluxes. This distinction strengthens the interpretation of flood-related environmental changes, highlights uncertainties associated with heterogeneous datasets and supports more consistent comparisons across spatial and temporal scales.

Table 7: Cross-sensor pixel correspondence between classified optical and radar water masks

NDWI date	S1 date	Δt (d)	Overlap (10^6 px)	Overall agreement (%)	Cohen's κ	Water-class IoU (%)	Water-class F1 (%)
2 April 2024	2 April 2024	0	3.36	96.6	0.54	38.3	55.4
14 April 2024	14 April 2024	0	3.66	88.4	0.65	56.3	72.0
18 April 2024	19 April 2024	1	2.39	91.5	0.65	53.0	69.3
Pooled	—	—	≈9.4	92.1	0.65	53.3	69.5

Note: The overlap denotes each shared comparison footprint; pairwise overlaps sum to 9.41 million pixels after rounding; the pooled overlap is therefore reported as approximately 9.4 million. These metrics describe classification correspondence, not independent mapping accuracy, and do not assess the 11 April maximum

Table 8: Optical–radar classification contingency for 14 April 2024 (thousands of pixels) within the reported common coverage

Optical NDWI class	SAR: water	SAR: non-water	Total, NDWI
NDWI: water	547.0	379.0	926.0
NDWI: non-water	45.6	2688.5	2734.1
Total, SAR	592.5	3067.5	3660.0

Note: Optical NDWI is the comparison label, not independent ground truth; cell entries and margins were rounded separately and may differ by 0.1 thousand pixels.

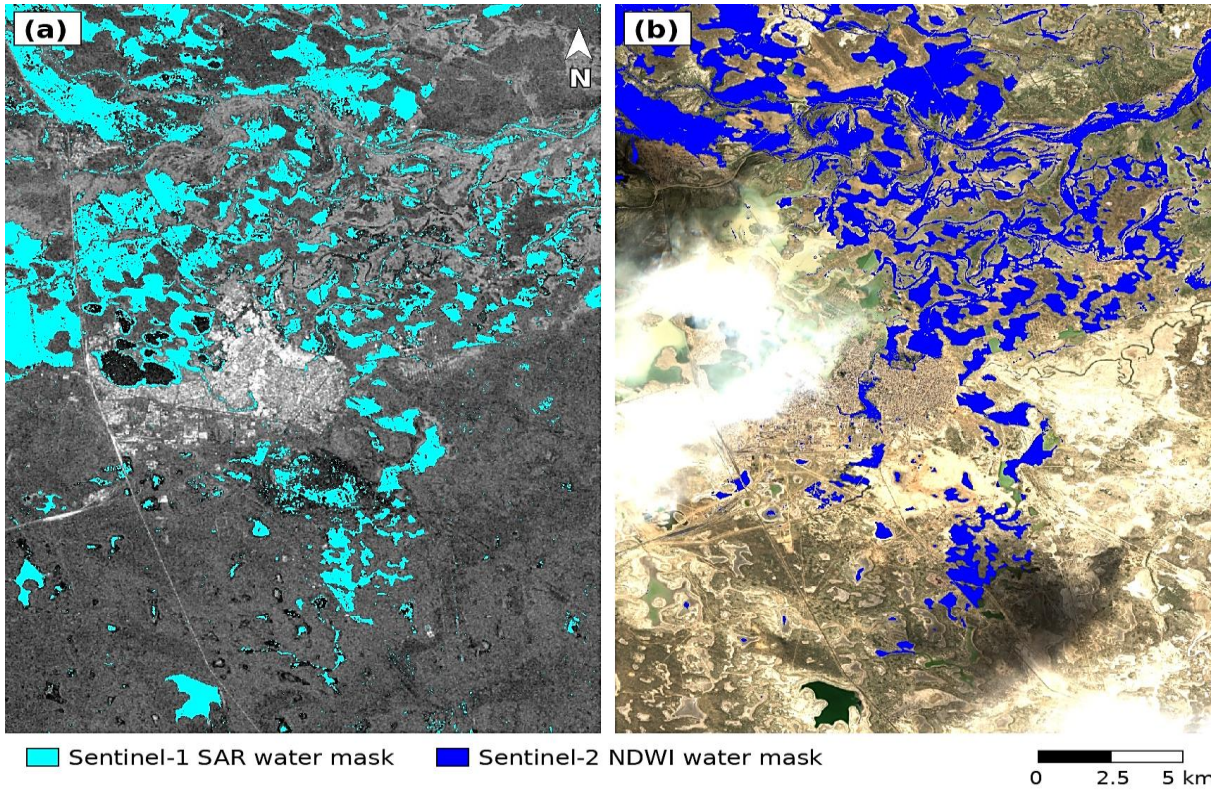

Fig. 5: The two water products for 14 April 2024, shown separately: (a) Sentinel-1 VV backscatter with the change-detection SAR water mask in cyan; (b) near-coincident Sentinel-2 true-color composite with the NDWI mask in blue. Cloud-affected optical pixels may alter the NDWI classification. The two panels have separate map layouts and are not co-registered to a common frame, so they illustrate the appearance and extent of each product individually and are not intended for pixel-by-pixel comparison; the quantitative comparison between the two products is given in Tables 7 and 8.

Interpreting flood expansion without attributing an unmeasured mechanism

The available evidence indicates marked expansion of classified surface water around Kulsary during a period of substantial flooding, with a contrast between lower-basin station conditions and published upstream snowmelt context (Laiskhanov *et al.*, 2025). Aligning the April 2 upstream stage maximum with the local classified-area sequence establishes temporal sequencing rather than a physically routed hydrograph. The 9- and 12-day offsets to the observed regional and subset maxima differ because the footprints, sensors and acquisition schedules differ. Frequent surface freeze–thaw cycles can occur alongside varying infiltration behavior, depending on subsurface soil ice content, moisture distribution, and hydraulic structure (Gray *et al.*, 2001; Mohammed *et al.*, 2018; Zhao and Gray, 1999; Granger *et al.*, 1984). The environmental interpretation is therefore a scale-aware comparison of water extent, local weather and sampled groundwater state. Fig. 6 illustrates the observational data and candidate hydrological pathways within a structured conceptual framework. The groundwater-depth distribution demonstrates variation among urban monitoring locations. Depth multiplied by assumed SY does not establish the pore deficit accessible to floodwater. Consequently, well observations serve as a complementary environmental state indicator to the surface-water chronology, whereas event-dated head fluctuations and exchange measurements are required to quantify net recharge or groundwater discharge (Ma *et al.*, 2024).

Comparison with the wider basin and other settings

Laiskhanov *et al.* (2025) reported 836.8 km² of mapped inundation on 11 April 2024 over a different, larger basin-scale analysis area. The 622.35 km² value reported here is the classified surface-water area within the present regional footprint on the same date. Although differing denominators and methodological frameworks preclude direct quantitative validation of the respective inundated areas, temporal concordance between datasets provides contextual support for the overarching chronology of the flooding event. The upstream study emphasized basin meteorological forcing, while the present analysis documents optical water classifications and groundwater heterogeneity at Kulsary. The evidence is complementary in spatial focus rather than mechanistically competing. Recurrent near-surface freeze–thaw variability, fine-textured deposits, saline groundwater and low relief are plausible local influences, but no effect size for these influences has been estimated. Groundwater and floodplain interactions have been documented in a range of low-relief and alluvial settings (Hughes *et al.*, 2011; Abboud *et al.*, 2018; Doble *et al.*, 2014; Nowinski *et al.*, 2012; Houspanossian *et al.*, 2023; Mirlas *et al.*, 2025). In these systems, however, establishing groundwater-driven inundation or water-entry limitations requires time-resolved groundwater head, infiltration or exchange measurements. Relying solely on Kulsary well measurements and hypothetical storage estimates is insufficient to resolve these flow pathways or prioritize them against overbank routing and channel conveyance. Regional observations of shallow saline groundwater provide a relevant context for Kulsary (Ongayev *et al.*, 2026; Adenova *et al.*, 2025). Broader climate-related projections (Yu *et al.*, 2019) may motivate future assessments, but the single 2024 event and selected comparison years analyzed here do not support quantitative inference about future frequencies of flood-generating freeze–thaw sequences under changing climatic conditions across semi-arid regions.

Table 9: Urban well measurements and conditional water-table equivalent indices in 2024

Well	Depth to water (m) measured	Mineralización (g/L) measured	Water-level elevation (m) measured	I (mm), Sy = 0.05	I (mm), Sy = 0.10
300	3.42	10.7	−15.18	171.0	342.0
301	2.39	7.4	−13.91	119.5	239.0
302	2.37	4.6	−12.97	118.5	237.0
303	4.67	6.0	−13.99	233.5	467.0
304	3.12	8.1	−13.77	156.0	312.0
305	1.38	5.1	−12.03	69.0	138.0
306	0.37	1.8	−10.29	18.5	37.0
307	0.91	9.2	−12.56	45.5	91.0
308	3.25	8.9	−14.29	162.5	325.0
309	2.35	8.8	−14.29	117.5	235.0
310	5.53	2.8	−17.05	276.5	553.0
311	2.46	1.9	−13.99	123.0	246.0
312	1.95	2.5	−12.05	97.5	195.0
314	3.12	6.5	−13.55	156.0	312.0
316	3.75	10.9	−13.97	187.5	375.0
317	0.86	21.6	−13.85	43.0	86.0

Note: I = 1,000 × d × Sy, where d is measured in depth to water in meters and Sy is an assumed dimensionless SY. The final two columns are conditional indices in millimeters, not measured storage, recharge or infiltrable capacity.

Table 10: Observational assessment of local meteorological context (Q1), antecedent soil-surface temperature (Q2) and urban groundwater plus classified-water chronology (Q3)

Research question	Criterion applied	Evidence	Outcome	Principal limitation
Q1. Local meteorological context	2024 rank within station-specific snow and precipitation records	Kulsary ranks: snow 7/10; precipitation 6/10. Upstream stage maximum: 2 April (Laiskhanov *et al.*, 2025)	Local seasonal values were not record maxima; upstream-to-local chronology is documented	No discharge-based source partition
Q2. Antecedent freeze–thaw	Common 1 March–5 April window in four selected years	2024: 11 mean-freezing and 20 freeze–thaw days; 2022: 12 and 21	Thermal conditions were not unique within the selected subset	No full-decade eligibility screen or measured soil permeability
Q3. Groundwater state and water-area chronology	Sampled well depths, conditional indices and dated area changes	Depth 0.37–5.53 m; water-area maxima at +9 and +12 d; subset contraction 63.96%	Site heterogeneity and calendar ordering quantified; drainage and groundwater exchange unresolved	Unverified map accuracy and common masks; no synchronous hydraulic records

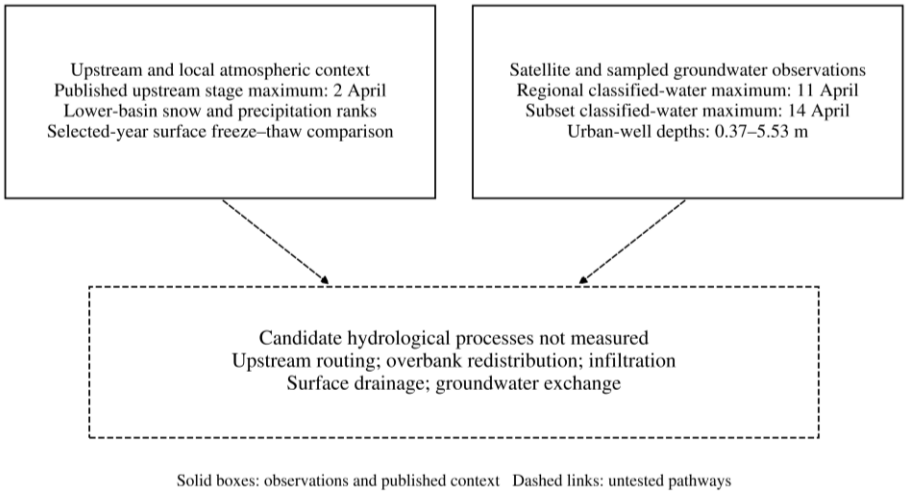

Fig. 6: Conceptual framework distinguishing observed or published conditions from candidate hydrological processes. Solid boxes contain observations and context; dashed boundaries and links denote untested pathways rather than demonstrated causation

Limits of flood recession and groundwater attribution

Within the 341 km² PlanetScope subset, classified-water area declined by 47.06 km² between 14 and 18 April and then changed by only 0.52 km² by 20 April; these repeated observations quantify apparent area contraction, not water loss or drainage discharge. In isolation, these observational scenes are insufficient to determine whether the surface water migrated downstream, infiltrated into the subsurface, evaporated, fragmented into isolated surface pools, or simply fell below the sensor detection threshold. Dated water-surface elevations and river or drainage-flow measurements are required to resolve the surface contribution; continuous well heads, hydraulic gradients and exchange or infiltration measurements are needed to resolve the subsurface contribution (Nowinski *et al.*, 2012; Peña *et al.*, 2022; Ma *et al.*, 2024); vegetation and channel roughness may also modify conveyance, but their effects require local geometry and hydraulic observations (Barinas *et al.*, 2024).

Limitations

The principal mapping constraints are the absence of independent reference labels, untested threshold sensitivity, unverified PlanetScope asset-band provenance and unequal valid observation coverage. The 622.35 km² observation includes pre-existing water, and the five-year archive does not establish comparable annual flood peaks. Ensuring reproducibility requires comprehensive documentation of scene identifiers, acquisition timestamps, quality-mask logs, common-footprint denominators, and radar preprocessing parameters. Furthermore, establishing a sample reference assessment and a persistent-water baseline is prerequisite to reporting flood-extent area or classification confidence limits. The four-year thermal subset cannot establish a decade-wide freeze–thaw ranking. Event-relative well dates, well coordinates, topographic transects and time-resolved river discharge were not resolved, precluding spatial exchange estimates, hydraulic lag analysis and a coupled water balance. These constraints restrict the spatial or contextual applicability of the assessment rather than serving as numerical bounds of uncertainty.

Implications for research and flood monitoring

The case motivates environmental monitoring that combines upstream stage and discharge with validated satellite water change, flood duration, exposed land uses and local groundwater conditions; an operational framework would first verify persistent-water exclusion and common valid footprints, then align repeated optical and radar classifications with gauge hydrographs and continuously logged floodplain wells. Integrating depth-resolved measurements of soil temperature, moisture, and infiltration alongside hydrochemical tracers would effectively discriminate between candidate hydrological mechanisms and water sources (Ma *et al.*, 2024). Any improvement in warning performance should be assessed in independent flood and non-flood years against a benchmark based on upstream stage and catchment meteorology. Wells 306, 307 and 317 justify targeted site inspections; drainage-investment priorities additionally require exposure, duration and hydraulic-feasibility evidence.

CONCLUSION

The April 2024 Kulsary flood coincided with the largest classified surface-water extent in the available 2021–2025 Sentinel-2 record: 622.35 km² on 11 April, 5.6 times the mean of the other four annual mapped maxima. This output represents a descriptive optical classification rather than an independently verified extent of novel inundation or a historical flood benchmark. Furthermore, localized snow depth and March–April precipitation at the three lower-basin stations were within typical historical ranges, contrasting with documented evidence of deeper snowpacks and elevated winter precipitation in the upper basin. The relative contributions of upstream and local runoff cannot be determined without an event-specific water balance. Near-

surface thermal measurements indicate recurrent March freeze–thaw cycles in 2024 that are comparable to those observed in 2022, thereby precluding the identification of a unique frozen-soil infiltration mechanism. The sixteen urban groundwater wells indicate pronounced variation in groundwater depth, but specific-yield-based scenario calculations do not measure event-time infiltration or establish floodplain-wide storage sufficiency. Although optical and radar classifications demonstrate moderate water-class correspondence across three matched acquisition pairs, none of which capture the 11 April maximum; an independent assessment of peak-date accuracy remains necessary. The contraction of classified water area within the PlanetScope subset does not directly measure drainage efficiency. Collectively, the empirical evidence highlights a pronounced meteorological discrepancy between upstream and local domains, significant satellite-detected surface-water expansion, and heterogeneous urban groundwater dynamics, whilst leaving the individual contributions of infiltration, floodplain storage and drainage unresolved. The spatial contrast across observation systems is a central finding rather than a sufficient explanation of the flood mechanism. While the stations comparisons characterize meteorological inputs exclusively at three lower-basin locations; they are insufficient to quantify upstream river discharge volumes or transit times. The satellite chronology identifies a marked expansion and subsequent contraction in classified water within distinct regional and urban analysis footprints, but those mapped areas do not constitute independently verified floodwater volume, nor do they separate permanent water from newly inundated surfaces. Similarly, the wells document a broad local range of water-table depths but not the temporal hydraulic response to the flood. Conditional scaling via an assumed SY is insufficient to quantify actual subsurface storage volumes or determine the proportion of inundation driven by infiltration-excess mechanisms. The optical–radar comparison is informative about classification agreement on three available dates, yet it is neither an independent accuracy assessment nor a validation of the observed 11 April maximum. Future investigations should integrate consistent pre-event water masks, standardized usable-area denominators, temporally aligned river-stage measurements, depth-resolved soil thermal profiles, and event-synchronous groundwater monitoring. Such observations would enable rigorous testing—rather than presupposition—of competing hydrological pathways involving upstream inflow, floodplain redistribution, restricted infiltration, and surface–groundwater exchange, thereby strengthening evidence-based interpretation of flood-related hydrological processes. Until such measurements are available, the most defensible conclusion is that an unusually large mapped regional water area occurred alongside locally heterogeneous ground conditions and non-extreme lower-basin seasonal meteorological indicators; the partitioning of their contributions to the flood remains unresolved.

AUTHOR CONTRIBUTIONS

A. Umirbayeva, the principal investigator, conceived and designed the study, investigated the April 2024 Kulsary flood, collected and curated the research data, interpreted the findings, drafted the manuscript, supervised the research, administered the project and acquired funding. E. Orynbassarova contributed to conceptualization and methodology, implemented the software, processed and analyzed geospatial data, participated in the investigation and data curation, prepared maps and scientific visualizations, interpreted the results, and reviewed and edited the manuscript. Y. Auyelkhan validated the results, assessed their reliability and consistency, and reviewed and edited the manuscript. N. Saburova provided research resources and supporting data, prepared scientific visualizations, and reviewed and edited the manuscript. Y. Pangaliyev reviewed and approved the final manuscript. All authors reviewed and approved the manuscript.

ACKNOWLEDGEMENT

The authors acknowledge the National Hydrometeorological Service of Kazakhstan (Kazhydromet) for providing the meteorological observations used in this study. The research was supported by the Science Committee of the Ministry of Science and Higher Education of the Republic of Kazakhstan under the Zhas Galym program [Grant No. AP25795283], through the project entitled "Development of Web-GIS for Monitoring Surface Waters During Spring Floods Using Earth Remote Sensing and GIS Technologies."

CONFLICT OF INTEREST

The authors declare that there is no conflict of interest regarding the publication of this manuscript. In addition, ethical issues, including plagiarism, informed consent, misconduct, data fabrication and/or falsification, double publication and/or submission, and redundancy, were observed by the authors.

OPEN ACCESS

©2027 The author(s). This article is licensed under a Creative Commons Attribution 4.0 International License, which permits use, sharing, adaptation, distribution and reproduction in any medium or format, as long as you give appropriate credit to the original author(s) and the source, provide a link to the Creative Commons license, and indicate if changes were made. The images or other third-party material in this article are included in the article's Creative Commons license, unless indicated otherwise in a credit line to the material. If material is not included in the article's Creative Commons license and your intended use is not permitted by statutory regulation or exceeds the permitted use, you will need to obtain permission directly from the copyright holder. To view a copy of this license, visit: http://creativecommons.org/licenses/by/4.0/.

PUBLISHER'S NOTE

GJESM Publisher remains neutral regarding jurisdictional claims in published maps and institutional affiliations.

NEGATIVE AI STATEMENT

The author(s) declare that no AI tools or services were not used or not highly applied during the preparation of this work.

ABBREVIATIONS

%	Percent
°C	Degree Celsius
<	Less than
≤	Less than or equal to
>	Greater than
×	Multiplication sign
Δt	Time separation between paired satellite acquisitions
κ	Cohen's kappa agreement coefficient
10^6 px	One million pixels
AI	Artificial intelligence
AOI	Area of interest (in satellite map annotations)
B2	Band 2; green in a four-band PlanetScope product
B3	Band 3, Sentinel-2 green band
B4	Band 4; NIR in a four-band PlanetScope product, green in an eight-band product
B8	Band 8; Sentinel-2 NIR and eight-band PlanetScope NIR
CC BY	Creative Commons Attribution license
cm	Centimeter
d	Depth to groundwater in Eq. 2; day in acquisition intervals
dB	Decibel
DOI	Digital object identifier
ESA	European Space Agency
F1	Harmonic mean of precision and recall
g/L	Grams per liter
GIS	Geographic information system
GRD	Ground Range Detected (radar product)

Green	Green-band spectral reflectance in NDWI
I	Conditional water-table equivalent index
IoU	Intersection over union (water-class overlap statistic)
IW	Interferometric Wide (radar swath mode)
km	Kilometer
km²	Square kilometer (area unit)
km²/d	Square kilometers per day (mapped area change rate)
L2A	Level-2A surface reflectance product
m	Meter
mm	Millimeter
MSI	MultiSpectral Instrument
NA	Not available
NDWI	Normalized difference water index
NIR	Near-infrared
ORCID	Open Researcher and Contributor Identification
PBC	Public benefit corporation (corporate designation)
px	Pixel
Q1	Research question 1
Q2	Research question 2
Q3	Research question 3
S1	Sentinel-1 satellite mission
SAR	Synthetic aperture radar
SD	Standard deviation
Sy	Specific yield (dimensionless drainable-storage fraction)
Tmax	Daily maximum soil-surface temperature
Tmean	Daily mean soil-surface temperature
Tmin	Daily minimum soil-surface temperature
Tsoil	Mean soil-surface temperature
URL	Uniform resource locator
VV	Vertical–vertical radar polarization

REFERENCES

Abboud, J.M.; Ryan, M.C.; Osborn, G.D., (2018). Groundwater flooding in a river-connected alluvial aquifer. J. Flood Risk Manage., 11(4): e12334 **(11 pages)**.

ACAPS, (2024). Kazakhstan: floods—briefing note, 23 April 2024. Assessment Capacities Project, Geneva, Switzerland **(4 pages)**.

Adenova, D.; Sapargaliyev, D.; Sagin, J.; Absametov, M.; Murtazin, Y.; Smolyar, V., (2025). Assessing groundwater and soil quality in West Kazakhstan amid climate impacts and oil industry contamination risks. Sci. Rep., 15(1): 6663 **(19 pages)**.

Adeyemo, T.; Kramer, I.; Levy, G.J.; Mau, Y., (2022). Salinity and sodicity can cause hysteresis in soil hydraulic conductivity. Geoderma. 413: 115765 **(8 pages)**.

Alfian, D.; Meilianda, E.; Achmad, A.; Syukri M., (2026). Integrating hydrodynamic modeling and multi-criteria decision support for flood risk management in coastal systems. Global J. Environ. Sci. Manage., 12(3): 1287-1310 **(24 pages).**

Arkhipkin, O.P.; Sagatdinova, G.N., (2016). The use of various optical and radar remote sensing data in operative space monitoring of flood in Kazakhstan. J. Sib. Fed. Univ. Eng. Technol., 9: 1045–1058 **(14 pages)**.

Barinas, G.; Good, S.P.; Tullos, D., (2024). Continental scale assessment of variation in floodplain roughness with vegetation and flow characteristics. Geophys. Res. Lett., 51: e2023GL105588 **(9 pages)**.

Depari, C.D.A., (2026). Exploring the factors influencing community adaptations to coastal flooding using the adaptive capacity framework. Global J. Environ. Sci. Manage., 12(4): 1663-1686 **(24 pages).**

Doble, R.; Crosbie, R.; Peeters, L.; Joehnk, K.; Ticehurst, C., (2014). Modelling overbank flood recharge at a continental scale. Hydrol. Earth Syst. Sci., 18: 1273–1288 **(16 pages)**.

Granger, R.J.; Gray, D.M.; Dyck, G.E., (1984). Snowmelt infiltration to frozen Prairie soils. Can. J. Earth Sci., 21: 669–677 **(9 pages)**.

Gray, D.M.; Toth, B.; Zhao, L.; Pomeroy, J.W.; Granger, R.J., (2001). Estimating areal snowmelt infiltration into frozen soils. Hydrol. Process., 15: 3095–3111 **(17 pages)**.

Houspanossian, J.; Giménez, R.; Whitworth-Hulse, J.I.; Nosetto, M.D.; Tych, W.; Atkinson, P.M.; Rufino, M.C.; Jobbágy, E.G., (2023). Agricultural expansion raises groundwater and increases flooding in the South American plains. Science. 380: 1344–1348 **(5 pages)**.

Hughes, A.G.; Vounaki, T.; Peach, D.W.; Ireson, A.M.; Jackson, C.R.; Butler, A.P.; Bloomfield, J.P.; Finch, J.; Wheater, H.S., (2011). Flood risk from groundwater: examples from a Chalk catchment in southern England. J. Flood Risk Manag., 4: 143–155 **(13 pages)**.

Johnson, A.I., (1967). Specific yield: compilation of specific yields for various materials. U.S. Geological Survey Water-Supply Paper 1662-D, U.S. Government Printing Office, Washington, DC, USA **(74 pages)**.

Laiskhanov, S.; Sharapkhanova, Z.; Myrzakhmetov, A.; Levin, E.; Taukebayev, O.; Nurmagambetuly, Z.; Kaster, S., (2025). Geo-ecological analysis of the causes and consequences of flooding in the western region of Kazakhstan. Urban Sci., 9: 20 **(19 pages)**.

Ma, R.; Chen, K.; Andrews, C.B.; Loheide, S.P.; Sawyer, A.H.; Jiang, X.; Briggs, M.A.; Cook, P.G.; Gorelick, S.M.; Prommer, H.; Scanlon, B.R.; Guo, Z.; Zheng, C., (2024). Methods for quantifying interactions between groundwater and surface water. Annu. Rev. Environ. Resour., 49: 623–653 **(31 pages)**.

McFeeters, S.K., (1996). The use of the normalized difference water index (NDWI) in the delineation of open water features. Int. J. Remote Sens., 17: 1425–1432 **(8 pages)**.

Mkilima, T.; Zhidebayeva, A.; Syrlybekkyzy, S.; Taizhanova, L.; Koibakova, S.; Altybaeva, Zh.; Koishina, A.; Seidaliyeva, L., (2027). From pixels to policy: a critical synthesis of remote sensing and GIS indicators for ecosystem and biodiversity monitoring. Environ. Eng. Res., 32(2): 250445 **(22 pages)**.

Mirlas, V.; Zhakyp, A.; Auelkhan, Y.; Anker, Y., (2025). Assessment of urbanization-related groundwater flooding process via Visual MODFLOW modeling: a case study for the northern part of Almaty city, Kazakhstan. J. Flood Risk Manage., 18: e13029 **(20 pages)**.

Mohammadi, A.; Costelloe, J.F.; Ryu, D., (2017). Application of time series of remotely sensed normalized difference water, vegetation and moisture indices in characterizing flood dynamics of large-scale arid zone floodplains. Remote Sens. Environ., 190: 70–82 **(13 pages)**.

Mohammed, A.A.; Kurylyk, B.L.; Cey, E.E.; Hayashi, M., (2018). Snowmelt infiltration and macropore flow in frozen soils: overview, knowledge gaps, and a conceptual framework. Vadose Zone J., 17(1): 180084 **(15 pages)**.

Munasinghe, D.; Cohen, S.; Huang, Y.-F.; Tsang, Y.-P.; Zhang, J.; Fang, Z., (2018). Intercomparison of satellite remote sensing-based flood inundation mapping techniques. J. Am. Water Resour. Assoc., 54: 834–846 **(13 pages)**.

Nowinski, J.D.; Cardenas, M.B.; Lightbody, A.F.; Swanson, T.E.; Sawyer, A.H., (2012). Hydraulic and thermal response of groundwater–surface water exchange to flooding in an experimental aquifer. J. Hydrol., 472–473: 184–192 **(9 pages)**.

Olofsson, P.; Foody, G.M.; Herold, M.; Stehman, S.V.; Woodcock, C.E.; Wulder, M.A., (2014). Good practices for estimating area and assessing accuracy of land change. Remote Sens. Environ., 148: 42–57 **(16 pages)**.

Ongayev, M.; Nasiyev, B.; Japarov, R.; Ayupov, Y.; Umbetkaliyev, N.; Denizbayev, S., (2026). Influence of flooding on soil properties and the agrobiological indicators of natural herbage in the farmlands of West Kazakhstan. Int. J. Agric. Biosci., 15(2): 378–389 **(12 pages)**.

Pekel, J.-F.; Cottam, A.; Gorelick, N.; Belward, A.S., (2016). High-resolution mapping of global surface water and its long-term changes. Nature, 540(7633): 418–422 **(5 pages)**.

Peña, F.; Nardi, F.; Melesse, A.; Obeysekera, J.; Castelli, F.; Price, R.M.; Crowl, T.; Gonzalez-Ramirez, N., (2022). Compound flood modeling framework for surface–subsurface water interactions. Nat. Hazards Earth Syst. Sci., 22: 775–793 **(19 pages)**.

Planet Labs PBC, (2026). Planet Imagery Product Specifications. June 2026 edition, Planet Labs PBC **(88 pages)**.

Xu, H., (2006). Modification of normalised difference water index (NDWI) to enhance open water features in remotely sensed imagery. Int. J. Remote Sens., 27: 3025–3033 **(9 pages)**.

Yu, Y.; Pi, Y.; Yu, X.; Ta, Z.; Sun, L.; Disse, M.; Zeng, F.; Li, Y.; Chen, X.; Yu, R., (2019). Climate change, water resources and sustainable development in the arid and semi-arid lands of Central Asia in the past 30 years. J. Arid Land, 11: 1–14 **(14 pages)**.

Zagidullina, A.R.; Kulebayev, K.M., (2024). Assessment of the relationship between surface and groundwater of the Syrdarya river (within Kazakhstan). Gidrometeorol. Ekol., 113(2): 7–15 **(9 pages)**.

Zhang, T., (2005). Influence of the seasonal snow cover on the ground thermal regime: an overview. Rev. Geophys., 43: RG4002 **(26 pages)**.

Zhidebayeva, A.; Syrlybekkyzy, S.; Taizhanova, L.; Koibakova, S.; Altybaeva, Z.; Koishina, A.; Seidaliyeva, L.; Mkilima, T., (2025). Emerging frontiers in ecosystem and biodiversity monitoring using remote sensing and geographic information systems. Global J. Environ. Sci. Manage., 11(4): 1791–1818 **(28 pages)**.

Zhao, L.; Gray, D.M., (1999). Estimating snowmelt infiltration into frozen soils. Hydrol. Process., 13(12–13): 1827–1842 **(16 pages)**.

AUTHOR (S) BIOSKETCHES

Umirbayeva, A., Associate Professor-Researcher, Head of the Department of Geodesy and Cartography, Cadastre, International Educational Corporation, Almaty 050043, Kazakhstan.
- Email: *a.umirbaeva@kazgasa.kz*
- ORCID: 0000-0002-4746-3411
- Web of Science ResearcherID: ECS-7921-2022
- Scopus Author ID: 57226885309
- Homepage: https://kazgasa.kz/

Orynbassarova, E., Ph.D., Associate Professor, head of the Geomatics Innovative Center, Satbayev University, Almaty 050013, Kazakhstan.
- Email: *e.orynbassarova@satbayev.university*
- ORCID: 0000-0001-6421-4698
- Web of Science ResearcherID: AAQ-9768-2020
- Scopus Author ID: 57205164606
- Homepage: https://satbayev.university/

Auyelkhan, Y., Candidate of Technical Sciences, Associate Professor, Director of the Geology and Oil-Gas Business Institute named after K. Turyssov, Satbayev University, Almaty 050013, Kazakhstan.
- Email: *y.auyelkhan@satbayev.university*
- ORCID: 0000-0002-7598-0088
- Web of Science ResearcherID: AEK-5594-2022
- Scopus Author ID: 57203119858
- Homepage: https://satbayev.university/

Saburova, N., Ph.D. Candidate, Department of Hydrogeology, Engineering and Petroleum Geology, Satbayev University, Almaty 050013, Kazakhstan.
- Email: *n.saburova@aggvoda.kz*
- ORCID: 0009-0000-9559-4822
- Web of Science ResearcherID: NA
- Scopus Author ID: NA
- Homepage: https://satbayev.university/

Pangaliyev, Y., Ph.D., Acting Associate Professor, Department of Ecology and Life Safety, Faculty of Engineering, Yessenov University, 32nd Microdistrict, 1, 130000, Aktau, Kazakhstan.
- Email: *yerbol.pangaliyev@yu.edu.kz*
- ORCID: 0000-0002-2392-4180
- Web of Science ResearcherID: MGB-2344-2025
- Scopus Author ID: 57191078212
- Homepage: https://eng.yu.edu.kz/en/pps-ekologiya/pangaliyev-yerbol/

HOW TO CITE THIS ARTICLE:
Umirbayeva, A.; Orynbassarova, E.; Auyelkhan, Y.; Saburova, N.; Pangaliyev, Y., (2027). Environmental floods assessment by integrating satellite-based water classifications with local hydroclimatic and groundwater observations. Global J. Environ. Sci. Manage., 13(2): …-…

DOI: https://doi.org/10.22034/gjesm.2027.02.11
URL: https://www.gjesm.net/article_736301.html